The Astronomical Journal, 164:181 (11pp), 2022 November https://doi.org/10.3847/1538-3881/ac8b7c

Carbon Abundance of Stars in the LAMOST-Kepler Field

Athira Unni[1,2], Mayank Narang[3], Thirupathi Sivarani[1], Manoj Puravankara[3], Ravinder K Banyal[1], Arun Surya[3], S. P. Rajaguru[1], and C. Swastik[1,2]
[1] Indian Institute of Astrophysics, Koramangala 2nd Block, Bangalore 560034, India; athira.u@iiap.res.in
[2] Pondicherry University, R.V. Nagar, Kalapet, 605014, Puducherry, India
[3] Department of Astronomy and Astrophysics, Tata Institute of Fundamental Research, Homi Bhabha Road, Colaba, Mumbai 400005, India
Received 2022 April 28; revised 2022 July 23; accepted 2022 August 12; published 2022 October 10

Abstract

The correlation between host star iron abundance and the exoplanet occurrence rate is well established and arrived at in several studies. Similar correlations may be present for the most abundant elements, such as carbon and oxygen, which also control the dust chemistry of the protoplanetary disk. In this paper, using a large number of stars in the Kepler field observed by the LAMOST survey, it has been possible to estimate the planet occurrence rate with respect to the host star carbon abundance. Carbon abundances are derived using synthetic spectra fit of the *CH- G*-band region in the LAMOST spectra. The carbon abundance trend with metallicity is consistent with the previous studies and follows the Galactic chemical evolution (GCE). Similar to [Fe/H], we find that the [C/H] values are higher among giant-planet hosts. The trend between [C/Fe] and [Fe/H] in planet hosts and single stars is similar; however, there is a preference for giant planets around host stars with a subsolar [C/Fe] ratio and higher [Fe/H]. Higher metallicity and subsolar [C/Fe] values are found among younger stars as a result of GCE. Hence, based on the current sample, it is difficult to interpret the results as a consequence of GCE or due to planet formation.

Unified Astronomy Thesaurus concepts: Stellar abundances (1577); Exoplanet formation (492); Spectroscopy (1558); Surveys (1671); Planet hosting stars (1242); Exoplanet catalogs (488)

Supporting material: machine-readable table

1. Introduction

Planets and their host stars are formed together from the same molecular cloud. Naturally, the planet's chemical composition is expected to correlate with the host star. Hence, studies of the host star's chemical abundances could constrain the planet's bulk abundance and the planet formation process. Host star metallicity and giant-planet connection was first observed by Gonzalez (1997, 1998) and confirmed by Santos et al. (2001, 2004) with a larger sample. These authors also showed that the frequency of giant-planet hosts increases steeply above solar metallicity. This rapid rise in giant planet ($R_p > 4R_{\oplus}$) occurrence of 3% at solar metallicities and up to 25% at [Fe/H] = 0.3 was again shown by Fischer & Valenti (2005). Johnson et al. (2010) observed giant-planet–metallicity correlation in a wide range of stellar masses, and the occurrence increased from 3% in M dwarfs to 14% in A dwarfs at solar metallicity. Although the metallicity trend was absent for stars that host smaller planets, a large spread in metallicities is observed among them (Sousa et al. 2008; Neves et al. 2009), and the low-mass planet-bearing stars at low metallicity were found to be rich in α elements (Adibekyan et al. 2012a, 2012b, 2012c; Mulders 2018). Adibekyan et al. (2012a) suggested terrestrial planets could form early in the galaxy among the thick disk stars due to their enhanced α abundances. A recent study by Swastik et al. (2022) showed that [α/Fe] ratio shows a negative trend with respect to planetary mass, indicating possible conditions for the formation of low-mass planets before Jupiter-like planets. The host star mass–metallicity trend was also found to reverse for planet masses higher than $M > 4M_J$ (Narang et al. 2018). Directly imaged planets also showed a large scatter in the metallicity among super Jupiters, indicating higher metallicity may not be necessary to form super Jupiters (Swastik et al. 2021).

The enhanced abundance of volatile elements as compared to refractory elements was first observed in the solar atmosphere (Meléndez et al. 2009), this could be used as a possible signature of the solar system among solar twins (Ramírez et al. 2009; Meléndez et al. 2012). However, high-precision differential abundances of solar analogs and stellar twins in binary systems did not show a significant difference in the trend of stellar abundance and condensation temperatures among planet hosts and nonhosts (Gonzalez et al. 2010; González Hernández et al. 2010, 2013; Mishenina et al. 2016). In fact, Adibekyan et al. (2014) noticed a significant correlation of the stellar abundances versus condensation temperature slope with stellar age and Galactocentric distance among Sun-like stars, which could be a cause for the observed difference in the volatile and refractive element abundances. Stellar lithium abundance could be a sensitive indicator of planet pollution; however, the results were inconclusive, showing a large spread in Li even among stars of very similar stellar parameters (Pollack et al. 1996; Israelian et al. 2009; Gonzalez et al. 2010; Delgado Mena et al. 2014, 2015; Figueira et al. 2014; Gonzalez 2014; Mishenina et al. 2016). Carbon is produced in massive stars similar to α elements at low metallicities, but low-mass asymptotic giant-branch (AGB) stars could also make carbon (Gustafsson et al. 1999; Kobayashi et al. 2020) at higher metallicities, and hence the C/O ratio can change with time. Bond et al. (2010) and Delgado Mena et al. (2010) showed the importance of C/O ratio in the formation of carbide and silicates in the planet formation and determine the planet mineralogy (Madhusudhan 2012). Ecuvillon et al. (2004) studied 91 planet hosts and 31 nonhost solar-type dwarf stars using

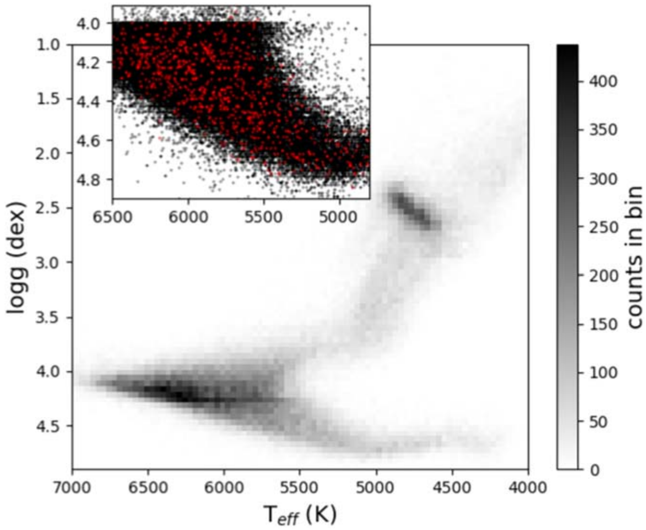

Figure 1. The entire sample from the LAMOST-KEPLER field is shown as a density plot. And the selected samples within the restricted stellar parameters for the current study is shown as an inset. The black and red dots indicate the field and the planet host stars, respectively.

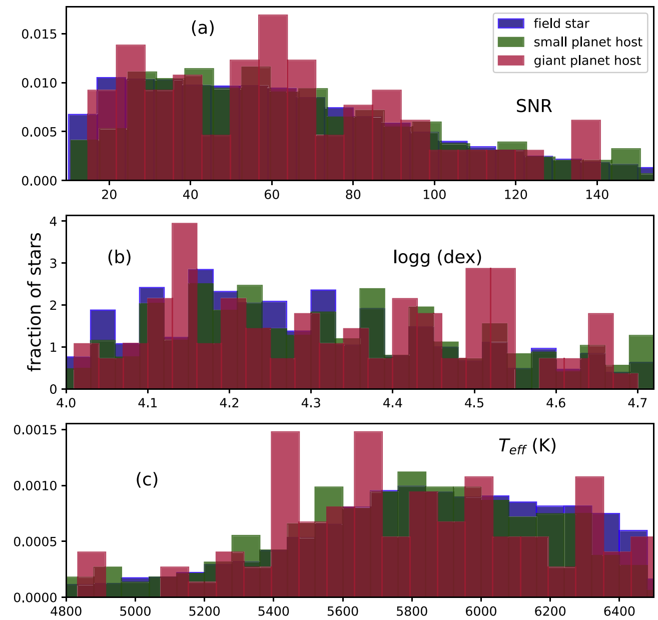

Figure 2. Distribution of S/N, T_{eff}, and log g of the final sample ($4800 \leqslant T_{\text{eff}} \leqslant 6500$ K and log $g \geqslant 4.0$). The small-planet host with planet radius $R_p \leqslant 4\,R_\oplus$, giant-planet($R_p > 4R_\oplus$) host stars and field stars are in green, red and blue respectively.

atomic carbon lines and found no significant difference in [C/Fe] for the planet host and the nonhost stars. Delgado Mena et al. (2010) also found no difference between carbon abundance between giant-planet hosts and nonhost stars. Suárez-Andrés et al. (2017) used the *CH*-band at 4300 Å for deriving the carbon abundance instead of the atomic lines at 5380.3 Å and 5052.2 Å to study the carbon abundance of HARPS FGK stars with 112 giant-planet hosts and 639 stars without known planets. Furthermore, they found that [C/Fe] is not varying as a function of the planetary mass, indicating the absence of a significant contribution of carbon in the formation of planets.

In this paper, we present the occurrence rate analysis of carbon abundance based on a large number of Kepler-LAMOST (The Large Sky Area Multi-Object Fiber Spectroscopic Telescope) samples of main-sequence FGK stars to understand the importance of carbon abundance in the context of planet formation process as well as Galactic chemical evolution (GCE) using the *CH G* band at 4300 Å. The sample contains 825 confirmed planet host stars and 214 stars with planet candidates from the Kepler catalog, and 49215 stars without detected planets so far.

2. Data and Target Selection

LAMOST is a wide field spectroscopic survey facility using a telescope with a 4 m clear aperture and 5° field of view. The survey obtains 4000 spectra in a single exposure to a limiting magnitude of $r = 19$ at the resolution $R = 1800$ and simultaneous wavelength coverage of 370–900 nm (Zhao et al. 2012). We have used the LAMOST-Kepler project Zong et al. (2018) Public Data Release 4 (DR4)[4] data for the current study. The observations were carried out between 2012 and 2017 and covered the entire Kepler field. A total of 227,870 spectra belonging to 156,390 stars were available in the database and out of which the spectroscopic parameters for 126,172 stars were available from the LASP pipeline (Luo et al. 2014). The spectra and the corresponding stellar parameters (e.g., T_{eff}, log g, [Fe/H] and radial velocity) were obtained from the LAMOST database. Additional parameters such as the mass and the radius of the planets are taken from the NASA Exoplanet archive[5] (Akeson et al. 2013). We restricted the analysis to the main-sequence stars ($4800 \leqslant T_{\text{eff}} \leqslant 6500$ K and log $g \geqslant 4.0$), leading to a final sample of 49,215 field stars and 1039 host stars with conformed exoplanets and potential candidates. Figure 1 shows the parameter range of the final LAMOST-Kepler sample. Figure 2 shows the signal-to-noise ratio (S/N), log g and T_{eff} histogram distribution of the final sample.

3. Estimation of Carbon Abundances

The methodology for estimating the carbon abundance uses a grid of synthetic spectra of varying carbon abundances across various stellar parameters and interpolates the model spectra to match the observed spectra. In this work we used Kurucz ATLAS9 NEWODF (Castelli & Kurucz 2003) stellar atmospheric models by Castelli & Kurucz (2003) and Turbospectrum (Alvarez & Plez 1998) spectrum synthesis code V19.1 (Plez 2012) for generating the synthetic spectra. The atomic and molecular line lists are the same as that of Lee et al. (2008) and Carollo et al. (2012) with minor updates to the hyperfine structure and inclusions of isotopes for the heavy elements. The synthetic grid covers a wavelength range 4200–4400 Å, which covers the CH molecule of the *G*-band region, which is sensitive to carbon abundance. The synthetic spectra cover a range in effective temperatures between $T_{\text{eff}} = 3500$ and 7000 K, with an increment of 250 K and log g range is between 0.0 and 5.0 dex with an increment of 0.5 dex and $[\text{Fe/H}] = -1.0$ –+0.5 dex (with 0.5 dex increment). Carbon abundance was varied over this stellar parameter range at every 0.1 dex step size. We used a python script for interpolation and χ^2 minimization between the observed and the model spectra.

[4] LAMOST DR4 complete data available at http://dr4.lamost.org/.

[5] https://exoplanetarchive.ipac.caltech.edu

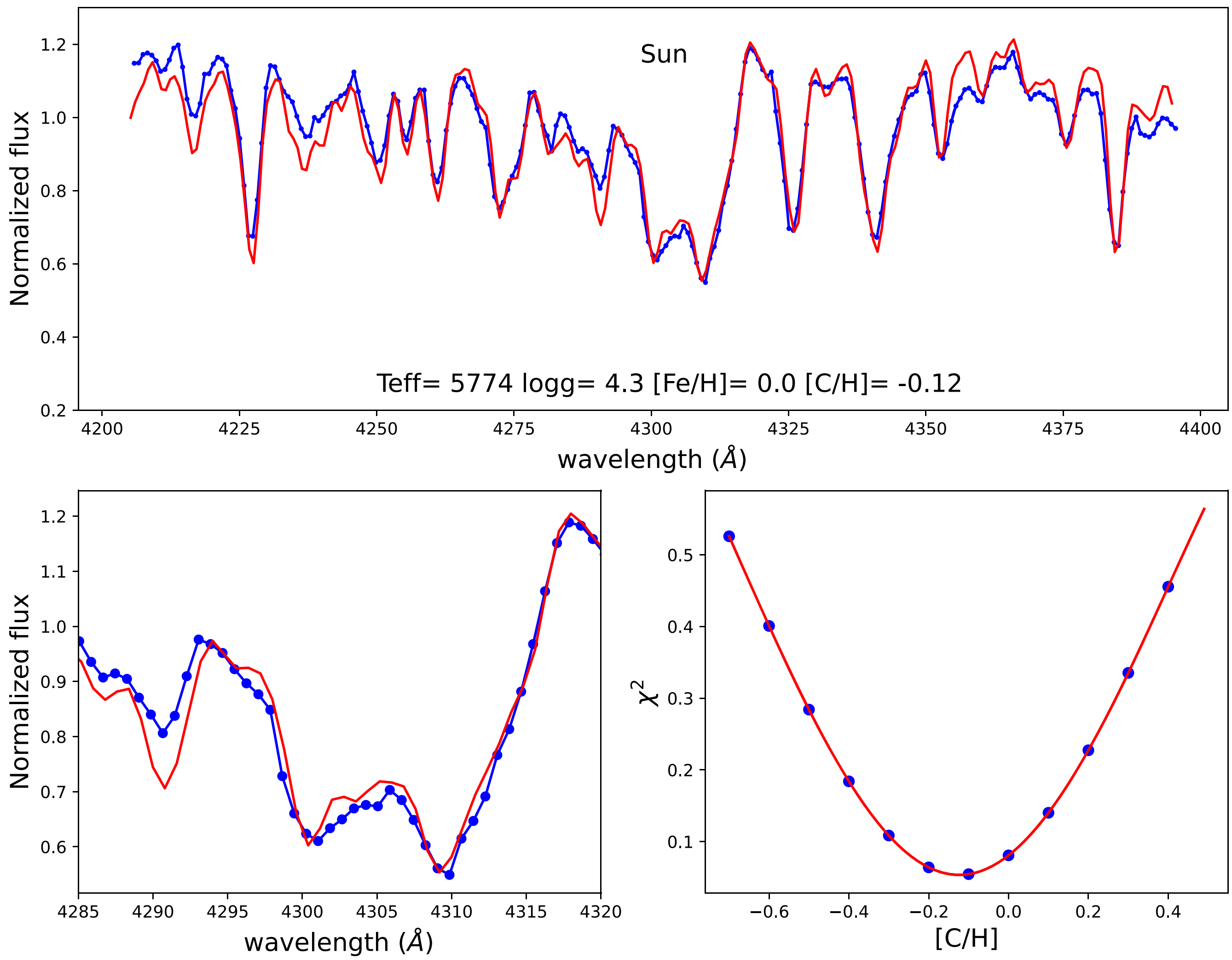

Figure 3. Observed spectra of Sun (blue) and the synthetic spectra (red). Top panel shows the best fit with input parameters from LAMOST. Bottom-left panel shows an enlarged view of the CH *G*-band region. Bottom right panel shows the χ^2 variation with [C/H] for obtaining the best-fit [C/H] value for the Sun with $T_{\rm eff} = 5774$ K and S/N = 76.

Since the wavelength coverage of the grid is limited, stellar parameters from LAMOST were used, and only the carbon abundances are varied for estimating the best fit between observed and synthetic spectra. Figure 3 shows an example of a best-fit spectrum. Solar scaled abundances are used for the stellar model atmospheres and synthetic spectra generation in the range [Fe/H] = +0.0 − +0.5 and for the metal-poor range, [Fe/H] = −1.0 − −0.5 dex an alpha enhanced abundances of [α/Fe] = 0.4 dex was used. Solar abundances values are taken from Grevesse et al. (2007) where $\log(N(C)/N(H)) + 12 = 8.39$ and $\log(N(O)/N(H)) + 12 = 8.66$ were used. The synthetic spectra grid uses an oxygen abundance ([O/H]) that scales with the metallicity for the metal-rich models ($0.0 < [Fe/H] < 0.5$) and follows the alpha abundance in the metal-poor models ([Fe/H] < 0.0), as expected by the GCE. We checked the sensitivity of the derived carbon abundances to the assumed oxygen abundance and found it has less impact on the current sample, as the targets have $T_{\rm eff} > 4800$ K and C/O < 1.0. We also visually inspected the goodness of the spectral fit for the entire planet host stars, using plots similar to Figure 3. Figure 4 represents the goodness of the fit at two extreme $T_{\rm eff}$ regime.

4. Carbon Abundances

The carbon abundances derived in this work use low-resolution spectra fitting the strong CH feature. We corrected the LAMOST carbon abundances using common samples from the California Kepler Survey (CKS; Brewer & Fischer 2018).[6] We have compared the derived carbon abundances with previous studies and found that the trend in carbon abundances with respect to [Fe/H] is consistent with APOGEE (Hawkins et al. 2016) and HARPS (Delgado Mena et al. 2010) data. We used 1025 common targets from CKS (Brewer & Fischer 2018) for deriving the corrections. As shown in Figure 5, the temperature scale between CKS and LAMOST common samples matches well after removing the 5σ outliers. First we made corrections to the CKS and LAMOST [Fe/H] estimates (from the LAMOST catalog), which is not significantly different (Figure 6). The LAMOST and CKS, [C/H] values show some dependency with effective temperature (Figure 7). So, in the next step, we derive corrections for [C/H] values as a function

[6] The CKS sample is available from https://doi.org/10.3847/1538-4365/aad501.

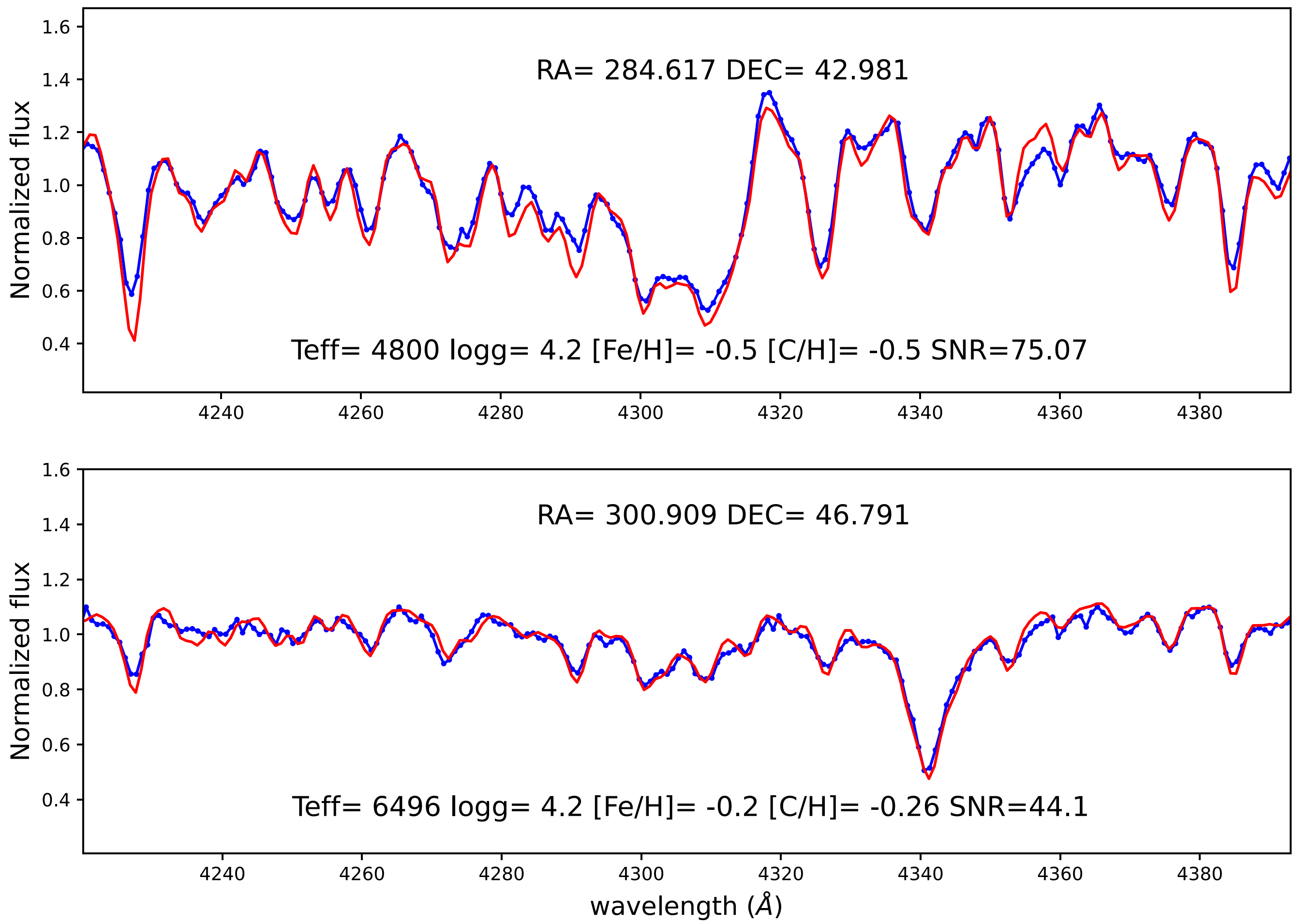

Figure 4. Observed spectra (blue) and synthetic spectra (red). Top panel shows the best fit for a star of $T_{\rm eff} = 4800$ K and S/N = 75.07. Bottom-left panel shows for the best fit for a star with $T_{\rm eff} = 6496$ K and S/N = 44.10.

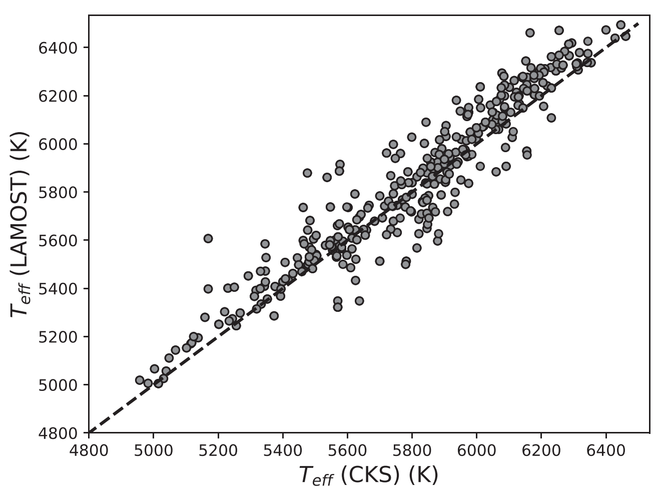

Figure 5. Comparison of the $T_{\rm eff}$ values from CKS and the LAMOST. The black line is the 1:1 line.

of $T_{\rm eff}$ (Figure 8). We verified the correction for Sun using HARPS solar spectra. We have used Sun as star spectra from HARPS and convolved and rebinned to LAMOST resolution. We also added Gaussian noise to the data with an S/N = 76, which is the mean S/N of the final sample. The stellar parameters we adopted for Sun are, $T_{\rm eff} = 5774$ K, log $g = 4.3$ dex and [Fe/H] = 0.0. We found an offset of $[{\rm C/H}]_{\rm LAMOST} = -0.12$ at solar temperature, which is consistent with the CKS corrections. The derived solar carbon abundance with CKS correction is $[{\rm C/H}]_{\rm LAMOST} = 0.09$ (Figure 3). In the following sections, we only use the CKS corrected LAMOST [Fe/H] and [C/H] values. The CKS corrected [Fe/H], [C/H] along with the stellar parameters of the sample stars are given in Table 1.

We plotted the derived carbon abundances with respect to the stellar parameters to infer any systematic trends among them. Figure 9 shows no obvious correlation between the derived carbon abundances with $T_{\rm eff}$ and log g. Figures 9(a) and (b) also shows no systematic difference in the $T_{\rm eff}$ and log g distribution between giant-planet host stars, small-planet host, and the field stars. The derived mean errors in the carbon abundances across different stellar parameters are also shown in the plots. The error in the carbon abundance is estimated from the χ^2 difference for a fixed difference $\delta[{\rm C/H}] = \pm 0.1$ dex in the carbon abundance around the minimum χ^2. Figure 9(c) represents [C/H] as a function of [Fe/H], that shows a positive trend between [Fe/H] and [C/H] as expected due to the GCE effect. Both [Fe/H] and [C/H] increase linearly from the low metallicity close to the solar value and then flatten. This is the typical behavior of α elements that indicate carbon is primarily produced due to massive stars. Carbon may start to increase slightly at the very metal-rich end due to carbon production from the AGB stars; however, it is

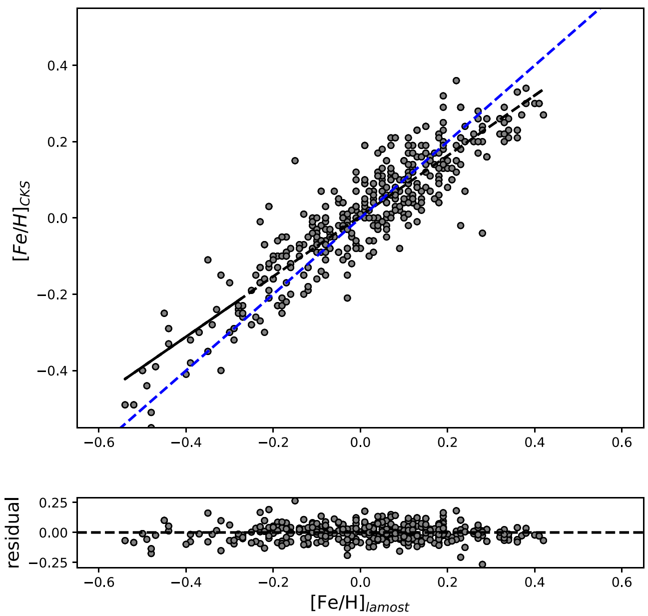

Figure 6. Comparison of the [Fe/H] values from CKS and the LAMOST pipeline. A linear fit is established between the CKS and the LAMOST [Fe/H] values. The best-fit coefficients are $[\mathrm{Fe/H}]_{\mathrm{new}} = [\mathrm{Fe/H}]_{\mathrm{lamost}} * 0.791 + 0.005$. The blue dashed line is the 1:1 line and black dashed line is the best-fit line.

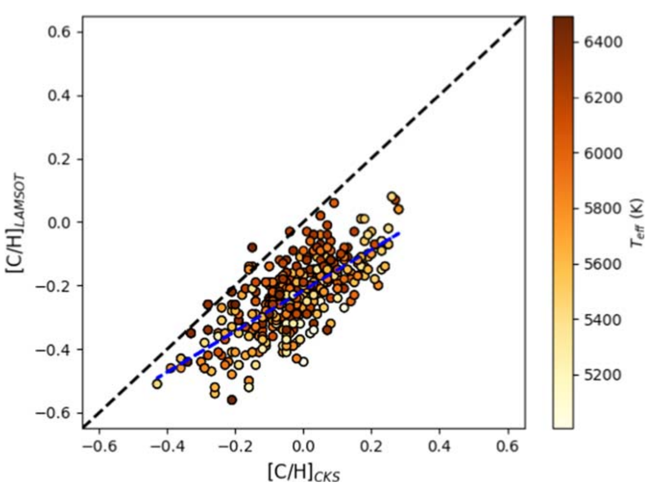

Figure 7. Comparison of the [C/H] values from CKS and the LAMOST as a function of T_{eff}. The black dashed line is the 1:1 line and blue dashed line is the best-fit line.

not very clear. Figure 9(d) represents the trend of [C/Fe] as a function of [Fe/H], which also represents the GCE effect of carbon with respect to iron. Both field stars and host stars follow a similar trend. From Figure 9(d), the mean value of [C/Fe] as a function of [Fe/H] shows that, small-planet host stars are preferentially found around higher [C/Fe] value in the metal-poor side ([Fe/H] < −0.2) compared to the field stars.

5. Results

We study the distribution of carbon abundance for planets of different radii and the occurrence rates with respect to the metallicity and carbon abundances. Using Galactic velocity dispersion, we infer the ages of the sample independent of the chemical abundances to understand the role of planet formation on the chemical composition.

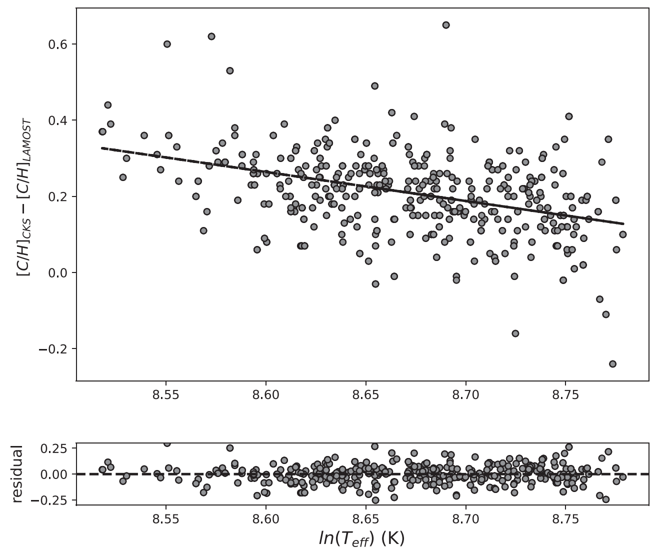

Figure 8. Comparison of $\delta[\mathrm{C/H}] = [\mathrm{C/H}]_{\mathrm{CKS}} - [\mathrm{C/H}]_{\mathrm{LAMOST}}$ as a function of T_{eff}. A linear fit is established and the best-fit coefficients are $\delta[\mathrm{C/H}] = -0.762 * \ln(T_{\mathrm{eff}}(\mathrm{lamost})) + 6.820$.

Table 1
Stellar Parameters and the Derived Carbon Abundance of the Sample Stars

R.A.(degree)	Decl.(degree)	T_{eff}	log g	[Fe/H]	[C/H]
12.9681	10.1142	5843.0	4.09	−0.5487	−0.2814
13.1028	8.7679	6058.0	4.34	0.0207	−0.0390
13.1220	9.1860	5044.0	4.57	−0.4775	−0.2193
13.1915	9.5228	5562.0	4.25	0.0681	0.0960
13.2336	8.7201	5401.0	4.57	−0.4854	−0.1415
13.2383	10.6629	5024.0	4.46	−0.0979	0.2636
13.2399	9.5898	5444.0	4.44	0.0444	-0.0075
13.2497	9.5943	5803.0	4.04	−0.5329	−0.3562
13.2887	9.7260	6266.0	4.11	−0.1928	−0.1047
13.3265	9.8816	5361.0	4.42	−0.4696	−0.2758
13.3561	11.1456	5858.0	4.44	0.0207	−0.0334
13.3963	9.6087	6201.0	4.03	−0.0662	−0.0568
13.4179	9.7623	6465.0	4.15	−0.3668	−0.3385
13.4460	9.7859	5720.0	4.34	−0.5566	−0.5352
…	…	…	…	…	…
…	…	…	…	…	…
…	…	…	…	…	…
303.2472	46.1495	5325.0	4.42	0.4082	0.3392
303.2586	45.8985	6281.0	4.50	−0.0662	0.1934
303.2754	45.9066	5685.0	4.21	0.1472	0.0194
303.2776	46.4944	5498.0	4.32	−0.3826	−0.3450
303.2888	45.2001	6111.0	4.17	0.0365	−0.0256
303.3010	45.4655	5548.0	4.21	0.1551	0.1180
303.3096	45.9596	5933.0	4.36	0.0365	−0.0331
303.3115	45.8891	6059.0	4.26	−0.0109	−0.0391
303.3131	46.2382	5750.0	4.09	0.1156	0.0007
303.3182	46.2866	6246.0	4.00	−0.1058	−0.0723
303.3222	45.8463	5833.0	4.00	−0.0662	−0.1701
303.3513	46.2210	6059.0	4.07	0.0760	−0.0091
303.3543	46.0936	5697.0	4.42	−0.0188	−0.0421
303.3627	45.4936	5605.0	4.05	−0.3193	−0.1597
303.3804	45.6495	5788.0	4.40	0.1077	−0.1142
303.3810	45.7701	6286.0	4.23	−0.0188	−0.2871
303.4039	45.6290	5910.0	4.25	−0.0109	0.1798

Note. Table 1 is published in its entirety in the machine-readable format. A portion is shown here for guidance regarding its form and content.

(This table is available in its entirety in machine-readable form.)

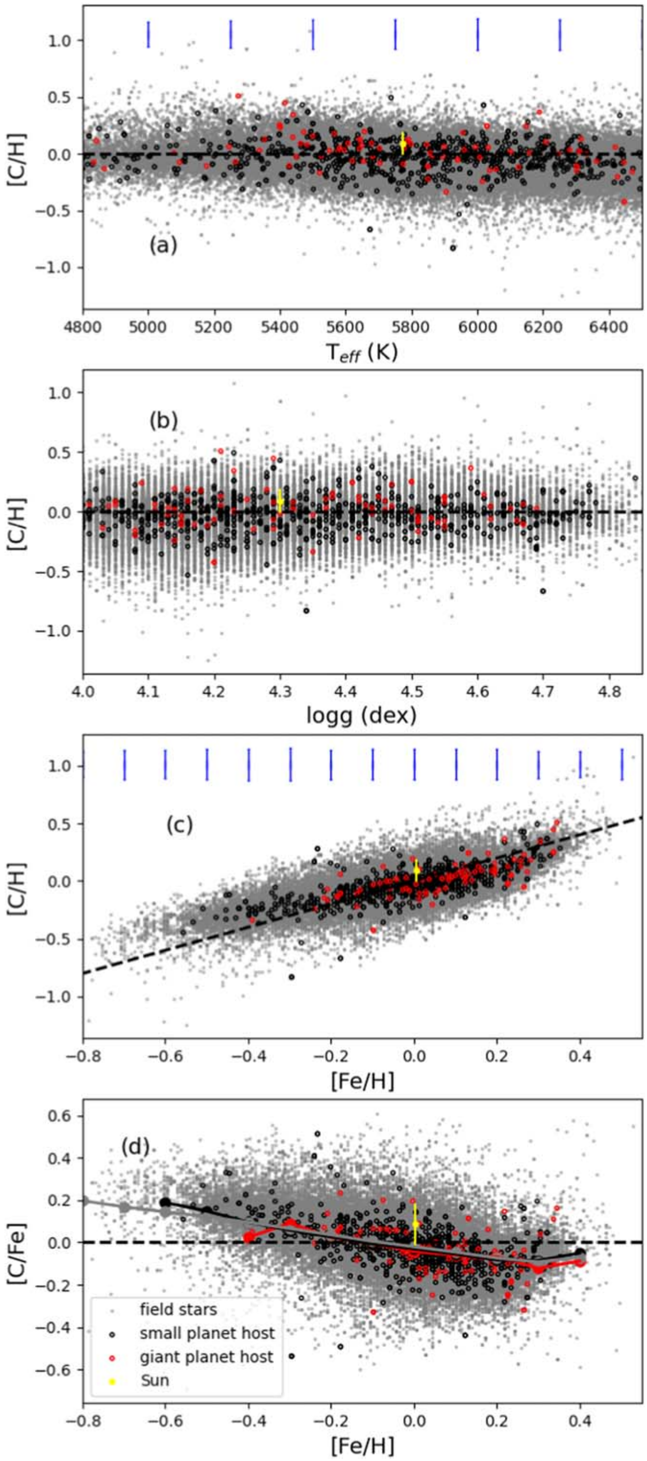

Figure 9. Variation in [C/H] as a function of T_{eff}(a), log g (b) and [Fe/H] (c) after CKS correction. Giant-planet host stars (red), small-planet host stars (black), field stars (gray), and Sun (yellow). Variation in [C/H] error (shifted for visual purpose at different x-values plotted in blue. In Figure 9(c), the black dashed line show the 1:1 correlation. (d) shows [C/Fe] as a function of [Fe/H] and the solid lines indicating the mean value of [C/Fe] in [Fe/H] bin of 0.2 dex for giant-planet host stars (red), Small-planet host stars (black) and field stars (gray).

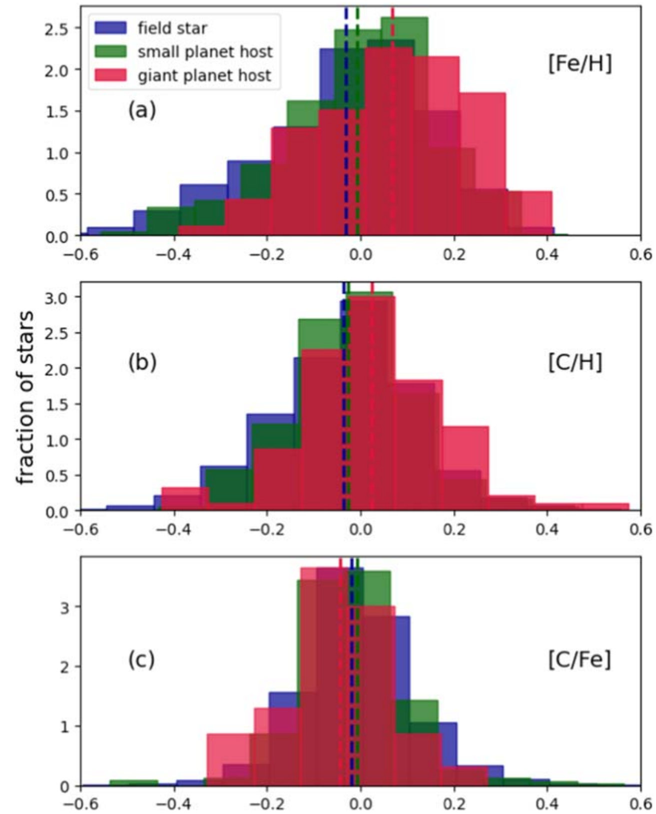

Figure 10. Distribution of carbon among small-planet($R_p \leqslant 4R_{\oplus}$) host, giant-planet($R_p > 4R_{\oplus}$) host stars and field stars. Dashed vertical line represents the mean value of each distribution.

Table 2
Main Results from the Histogram Distribution

Category	$[Fe/H]_{mean}$	$[C/H]_{mean}$	$[C/Fe]_{mean}$
Field star	-0.034 ± 0.001	-0.036 ± 0.001	-0.006 ± 0.001
Small-planet host	-0.006 ± 0.005	-0.025 ± 0.005	-0.019 ± 0.004
Giant-planet host	0.068 ± 0.016	0.023 ± 0.016	-0.044 ± 0.012

5.1. Elemental Abundance of the Host Stars as a Function of Planet Population

We examined the elemental abundance distribution of three distinct stellar populations: (i) host stars of the smaller planet ($R_p \leqslant 4\,R_{\oplus}$), (ii) host stars with giant planets ($R_p > 4\,R_{\oplus}$), and (iii) Kepler field stars with no known planet detection. Distributions of [Fe/H], [C/H], and [C/Fe] as a function of planetary radius is shown in Figure 10. We find that (a) giant-planet hosts, on average, have a higher value of $[Fe/H]_{mean}$ as compared to the host stars of small planets and the field stars. This indicates that the giant planets are preferentially found around metal-rich host stars, which is similar to previous studies (Mulders et al. 2016; Narang et al. 2018; Petigura et al. 2018). And even the smaller planet hosts have a slightly higher $[Fe/H]_{mean}$ as compared to the field stars, perhaps indicating that for the formation of small planets [Fe/H] could have some role (Schlaufman & Laughlin 2011).

Similarly in Figure 10(b), the distribution of [C/H] also follows similar trend as that of [Fe/H]. The giant-planet host stars are carbon-rich compared to field stars and small-planet host stars. The resulting [C/H] trend is expected because [C/H] increases with [Fe/H] due to GCE. However, the difference between the [C/H] distribution for small-planet hosts and field stars is insignificant. Figure 10(c) shows the distribution of [C/Fe] for host stars of different planet radii. We find [C/Fe] peaks at a

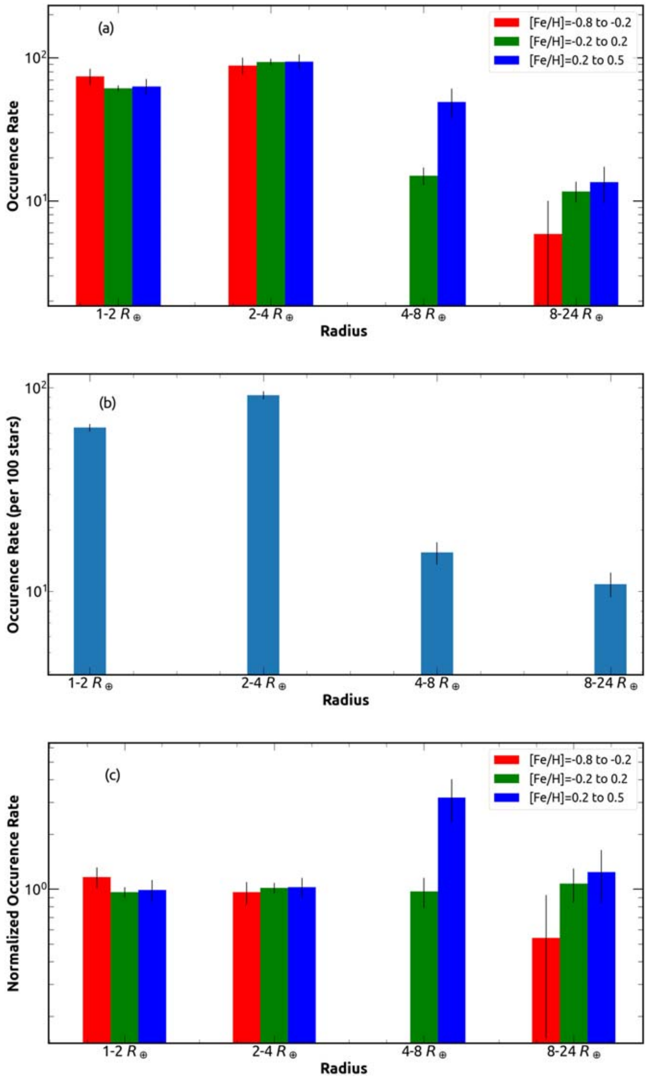

Figure 11. (a) Occurrence rate of exoplanets as a function of the planetary radius and the host star metallicity. (b) The total occurrence rate of the sample without subdividing it into different metallicity bins. (c) Normalized occurrence rate of the exoplanets as a function of the planetary radius and the host star metallicity. The error bars in these plots are the Poissonian errors based on the number of planets in each bin.

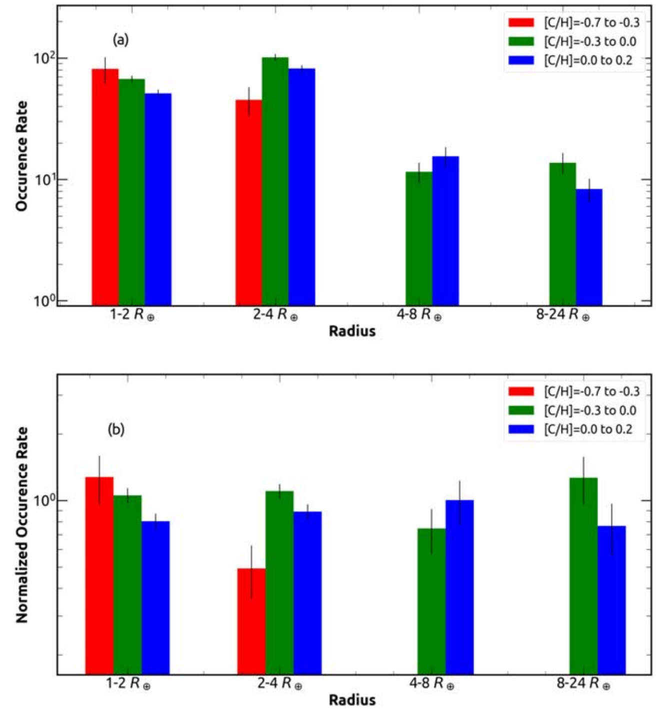

Figure 12. (a) Occurrence rate of exoplanets as a function of the planetary radius and the host star [C/H]. (b) Normalized occurrence rate of the exoplanets as a function of the planetary radius and the host star [C/H].

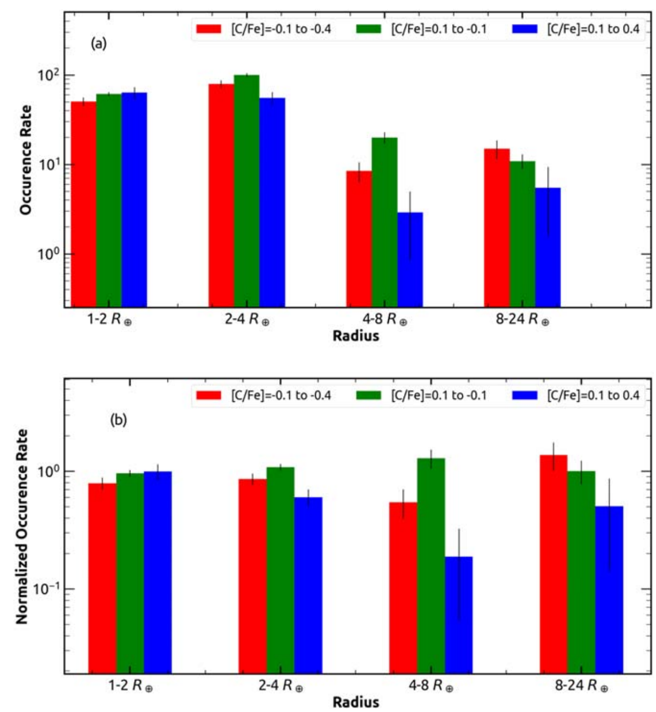

Figure 13. (a) Occurrence rate of exoplanets as a function of the planetary radius and the host star [C/Fe]. (b) Normalized occurrence rate of exoplanets as a function of the planetary radius and the host star [C/Fe].

higher value for the field stars compared to the planet hosts, which could be again due to the effect of GCE. Since most of the field stars are [Fe/H] poor compared to the planet hosts, the [C/Fe] at lower metallicities are expected to be higher, as most of the carbon in the galaxy seems to have come from massive stars and hence the [C/Fe] is high than solar values at lower metallicities (Kobayashi et al. 2020). Beyond solar metallicities, the rate of increase of iron is higher compared to carbon; hence the $[C/Fe]_{mean}$ value for the giant-planet host star is low compared to stars hosting small planets and field stars. The results are shown in Table 2.

5.2. *Occurrence Rate of Planets as a Function of Host Star Abundance*

The analysis described in the previous sections does not take the completeness of the Kepler survey, the detector efficiency, or the probability of detecting a planet into account. The real trend can not be inferred from histograms. In order to derive the correlation between the host star elemental abundance and the planet radius that is free of selection effects and observational biases, we use the final Kepler data release DR25 catalog Mathur et al. (2017, 2018)[7] to compute the occurrence rate of

[7] The Kepler DR25 data available at doi:10.3847/1538-4365/229/2/3, using the revision at doi:10.3847/1538-4365/aaa291.

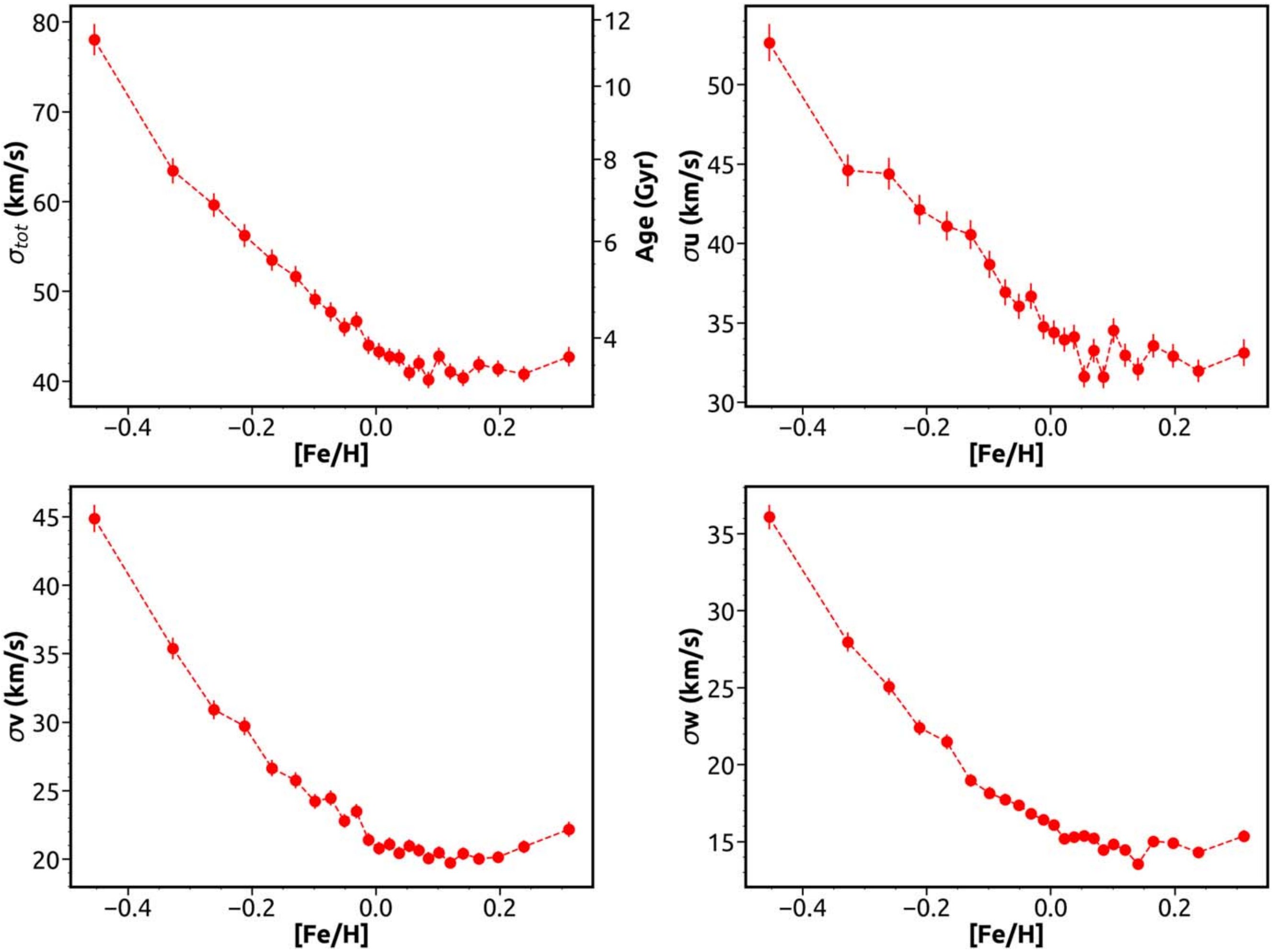

Figure 14. The total velocity dispersion and the velocity dispersion of the individual components (σ_U, σ_V, and σ_W) as a function of [Fe/H]. We have used a running average with a bin size of 1000 and a step size of 200. The error bar on the velocity dispersion are computed following Binney et al. (2000). On the right hand *y*-axis are the corresponding ages computed using Equation (4). The same axis and error bar as well as binning scheme is followed for all subsequent figures.

exoplanets as a function of radius and host star [Fe/H] and [C/H]. We updated the Kepler DR25 catalog with updated stellar and planetary radius based on Gaia DR2 from Berger et al. (2018). Since the LAMOST metallicity and the derived carbon abundances are calibrated with respect to the CKS values, we combine CKS samples (Brewer & Fischer 2018; Petigura et al. 2018) that has metallicities and carbon abundances. This also added additional samples for the occurrence rate estimation. To compute the occurrence rate as a function of planetary radii, we followed the prescription presented in Youdin (2011), Howard et al. (2012), Burke et al. (2015), and Mulders et al. (2016).

Similar to Narang et al. (2018), we have divided the sample into three [Fe/H] bins; (i) subsolar [Fe/H] ($-0.8 < [Fe/H] < -0.2$) , (ii) solar [Fe/H] ($-0.2 < [Fe/H] < 0.2$), and (iii) supersolar [Fe/H] ($0.2 < [Fe/H] < 0.8$). In Figure 11(a), the occurrence rate of the sample is shown as a function of planet radius and host star [Fe/H]. We also calculated the occurrence rate (for the exoplanet sample used in Figure 11(a) as a function of planet radius Figure 11(b). The 11(a), is both a function of host star [Fe/H] and radius. Similar to Narang et al. (2018), we normalized the occurrence rate in Figure 11(a) with the total occurrence rate as a function of radius Figure 11(b), to produce the normalized occurrence rate. The normalized occurrence rate Figure 11(c) is only a function of the host star [Fe/H]. From Figures 11(a) and 11(b) it can be seen that smaller planets $R_P \leqslant 4\,R_\oplus$ have similar occurrence rate for the three [Fe/H] ranges, while giant planets $R_P > 4\,R_\oplus$ have a higher occurrence rate for the solar and supersolar [Fe/H]. This is consistent with the previous works in literature (e.g., Mulders et al. 2016; Narang et al. 2018; Petigura et al. 2018).

To compute the occurrence rate of planets as a function of [C/H], we divided the sample into three [C/H] bins. Since we found that the [C/H] is a strong function of [Fe/H] (see Figure 13(c)) we converted the [Fe/H] bins to [C/H] bins. Based on equation

$$[C/H] = 0.657\ *\ [Fe/H] - 0.165 \qquad (1)$$

we define the bins as (i) subsolar [C/H] ($-0.7 < [C/H] < -0.3$), (ii) solar [C/H] ($-0.3 < [C/H] < 0.0$), and (iii) supersolar [C/H] ($0.0 < [C/H] < 0.2$). In Figure 12(a), the occurrence rate as a function of host star carbon abundance and planetary radius is shown. Similar to Figures 11(a), 12(a), is a strong function of both planetary radius and [C/H]. In Figure 12(b), the normalized occurrence rate of planets (using Figure 11(b)) as a function of [C/H] is shown. From Figure 12, we find that similar to Figure 11, the occurrence rate of giant planets is higher for stars with solar and supersolar [C/H].

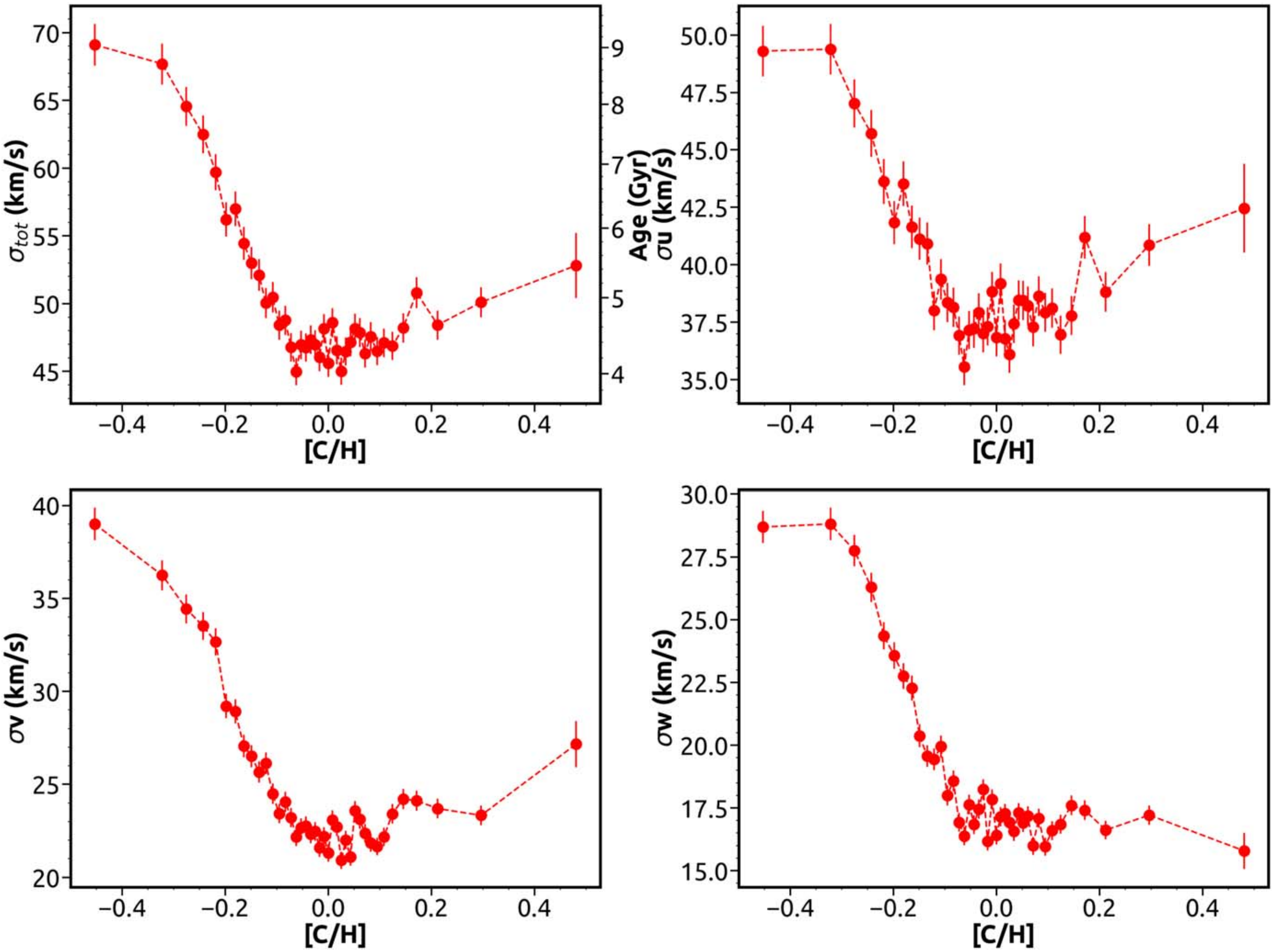

Figure 15. The total velocity dispersion and the velocity dispersion of the individual components (σ_U, σ_V, and σ_W) as a function of [C/H].

We further analyzed the occurrence rate of planets as a function of [C/Fe]. We divide the sample again into three bins (i) [C/Fe] between −0.4 and −0.1, (ii) [C/Fe] between −0.1 and 0.1, and (iii) [C/Fe] between 0.1 and 0.4. In Figure 13(a), the occurrence rate as a function of host star [C/Fe] and planetary radius is shown.We found that the occurrence rate for smaller planets ($R_P \leqslant 4\,R_\oplus$) is similar in all the three [C/Fe] bins, while the occurrence rate of the giant planets ($R_P > 4\,R_\oplus$) is much higher for [C/Fe] < 0.1. This might indicate that volatile elements such as carbon do not play a significant role in the formation of giant planets.

5.3. Galactic Space Velocity Dispersion

The increase in (normalized) occurrence rate as a function of [C/H] indicates that carbon enhancement is a necessary step in the Galactic context of planet formation, though it might not play a strong role as that of [Fe/H] in determining the size/radius of the planet. To further understand the planet population in the Galactic context, we need to understand the dependence and evolution of planetary properties and host star properties as a function of the Galactic age. In M.Narang et al. (2022, in preparation), we have established that the critical threshold of [Fe/H] in ISM that was necessary to form Jupiter-like planets was only achieved in the last 5–6 Gyr indicating that the Jupiters only started forming in the last 5–6 Gyr. Since the [C/Fe] values are expected to change over the timescale of the Galactic thin disk, we further investigated if probing the Galactic evolution of the [C/H] and/or the [C/Fe] might provide us with clues about the Galactic evolution of planetary systems. Similar to Binney et al. (2000), Manoj & Bhatt (2005), Hamer & Schlaufman (2019), and M. Narang et al. (2022, in preparation), we used the dispersion in the peculiar velocity of the stars as a proxy for the age of the stars in the Kepler field. We estimated the velocity dispersion (a proxy for the age) as function of [Fe/H], [C/H] and [C/Fe]. To compute the velocity dispersion, we first calculated the Galactic space velocity in terms of the *U, V*, and *W* space components following Johnson & Soderblom (1987) and Ujjwal et al. (2020). The total velocity dispersion ($\sigma_{\rm tot}$) for a particular ensemble of stars is then given as the quadratic sum of the individual components of the velocity dispersion in that given ensemble such that

$$\sigma_{\rm tot} = \sqrt{\sigma_U^2 + \sigma_V^2 + \sigma_W^2}, \tag{2}$$

where σ_U, σ_V, and σ_W are the velocity dispersion of the *U*, *V*, and *W* components given in the same manner as:

$$\sigma_U^2 = \frac{1}{N}\Sigma_{0=i}^{N}(U_i - \overline{U})^2. \tag{3}$$

Here, *N* is the number of stars.

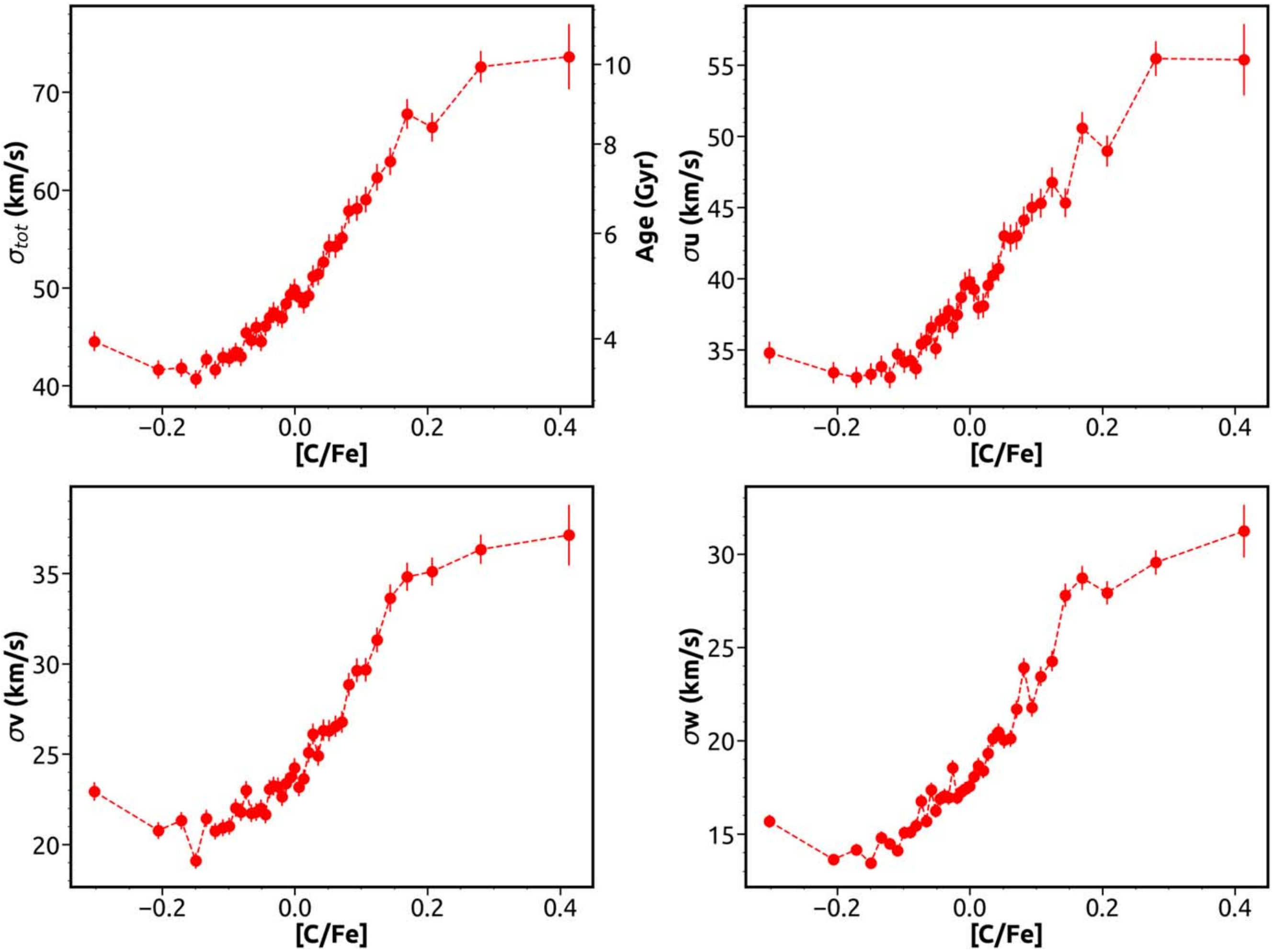

Figure 16. The total velocity dispersion and the velocity dispersion of the individual components (σ_U, σ_V, and σ_W) as a function of [C/Fe].

Furthermore velocity dispersion can then be converted to an average age of the stars following the formalism from M. Narang et al. (2022, in preparation):

$$\sigma_{\rm tot}(\tau) = A \times \tau^{\beta} \quad (4)$$

where τ is the average age of the host stars in a bin, A is a constant and is equal to $21.5\,{\rm km\,s^{-1}\,Gyr^{-0.53}}$, and $\beta = 0.53$.

In Figure 14, we show the velocity dispersion of the Kepler field as a function of [Fe/H]. As the average field [Fe/H] increases, the total velocity dispersion $\sigma_{\rm tot}$ decreases. This indicates that [Fe/H] rich stars ([Fe/H] > -0.2) are younger. Similar behavior is seen for the σ_U, σ_V, and σ_W as well. Using Equation (4), we can further convert $\sigma_{\rm tot}$ to the average age of the stars. We find that [Fe/H]-rich stars ([Fe/H] > -0.2) have an average age between ∼4 and 6 Gyr. Further from Figure 11, we find that most giant planets are around [Fe/H] rich stars. Hence from Figures 11 and 14 we conclude that most of the giant planets ($R_P > 4\,R_\oplus$) in the Kepler field are of an average age between ∼4 and 6 Gyr, while smaller planets have a much larger spread in host stars [Fe/H] and hence even in the age.

Similarly, by combining the results of velocity dispersion as a function of [C/H] from Figure 15 and the occurrence rate of planets in the Kepler field as a function of [C/H], we find that the average age of host stars of giant planets $R_P > 4\,R_\oplus$ is between 4 and 5 Gyr. Similar age ranges are obtained based on [C/Fe] as well (Figure 16).

6. Discussion

We have calculated the planet occurrence rate as a function of host star metallicity and carbon abundance. The distribution of [Fe/H] and [C/H] with respect to the planet radii show that planets with $R_p > 4\,R_\oplus$ are preferentially found around stars with solar and supersolar metallicities. At these preferred high metallicities, the GCE trend shows lower [C/Fe] ratios, and planet hosts also follow a similar trend as the field stars as shown in Figure 9. With the current sample, we do not find a significant difference in the [Fe/H] versus [C/Fe] trend above solar metallicities between the field stars and planet hosts. We explored the difference in [C/Fe] within a narrow bin in metallicity to remove the GCE trend; however, this has reduced the number of samples significantly. A simple mean gives a [C/Fe] value of −0.09 for field stars and −0.13 for giant-planet hosts for [Fe/H] > 0.28. However, at lower metallicities (where mostly low-mass planet hosts are present), the planet hosts may have slightly higher [C/Fe] values than the field stars, which is similar to what is observed in alpha elements (Adibekyan et al. 2012a). Hence, there may be a general preference for planet hosts to have higher abundances of metals. Since, planet hosts and field stars follow the GCE trends in elemental abundance, it is difficult to test the preference of a higher [C/Fe] among planet hosts at solar and supersolar metallicities. Stellar population with different abundance ratios with overlapping metallicity, similar to thick and thin disk, is not present at higher metallicity. Giant-planet frequency at a different Galactic distance from future microlensing surveys can cover a range of stellar metallicities and possibly with different abundance ratios.

7. Conclusion

We have used LAMOST-Kepler data of main-sequence dwarfs to derive the carbon abundance and compared the planet hosts and the field stars. We constrained the sample to the main-sequence dwarf stars to avoid effects due to stellar evolution. The distribution of carbon and iron with the planet radii and the occurrence rate analysis showed that the giant-planet hosts are metal-rich and carbon-rich compared to the field stars and the stars with smaller planets. However, at supersolar metallicities, the [C/Fe] values are lower than the solar ratio. At the metal-rich end, iron increases at a faster rate compared to carbon, which may be crucial for increasing the abundance of the refractory elements. Based on the Galactic space velocity dispersion, we found that the Jupiter host stars are younger, only about 4–5 Gyr old. From the detailed occurrence rate analysis, we found that carbon may not be a significant contributor to the mineralogy of planet formation as compared to iron.

We used LAMOST archival data and the NASA exoplanet archive for this study. Guoshoujing Telescope (the Large Sky Area Multi-Object Fiber Spectroscopic Telescope; LAMOST) is a National Major Scientific Project built by the Chinese Academy of Sciences. Funding for the project has been provided by the National Development and Reform Commission. LAMOST is operated and managed by the National Astronomical Observatories, the Chinese Academy of Sciences. We thank and acknowledge the immense contributions of Castelli in generating an extensive grid of stellar atmospheric models that this work used.

ORCID iDs

Athira Unni https://orcid.org/0000-0001-6093-5455
Mayank Narang https://orcid.org/0000-0002-0554-1151
Thirupathi Sivarani https://orcid.org/0000-0003-0891-8994
Manoj Puravankara https://orcid.org/0000-0002-3530-304X
Ravinder K Banyal https://orcid.org/0000-0003-0799-969X
Arun Surya https://orcid.org/0000-0002-9967-0391
S. P. Rajaguru https://orcid.org/0000-0003-0003-4561
C. Swastik https://orcid.org/0000-0003-1371-8890

References

Adibekyan, V. Z., Delgado Mena, E., Sousa, S. G., et al. 2012a, A&A, 547, A36
Adibekyan, V. Z., González Hernández, J. I., Delgado Mena, E., et al. 2014, A&A, 564, L15
Adibekyan, V. Z., Santos, N. C., Sousa, S. G., et al. 2012c, A&A, 543, A89
Adibekyan, V. Z., Sousa, S. G., Santos, N. C., et al. 2012b, A&A, 545, A32
Akeson, R. L., Chen, X., Ciardi, D., et al. 2013, PASP, 125, 989
Alvarez, R., & Plez, B. 1998, A&A, 330, 1109
Berger, T. A., Huber, D., Gaidos, E., & van Saders, J. L. 2018, ApJ, 866, 99
Binney, J., Dehnen, W., & Bertelli, G. 2000, MNRAS, 318, 658
Bond, J. C., O'Brien, D. P., & Lauretta, D. S. 2010, ApJ, 715, 1050
Brewer, J. M., & Fischer, D. A. 2018, ApJS, 237, 38
Burke, C. J., Christiansen, J. L., Mullally, F., et al. 2015, ApJ, 809, 8
Carollo, D., Beers, T. C., Bovy, J., et al. 2012, ApJ, 744, 195
Castelli, F., & Kurucz, R. L. 2003, in IAU Symp. 210, Modelling of Stellar Atmospheres, ed. N. Piskunov, W. W. Weiss, & D. Gray (San Francisco, CA: ASP), A20
Delgado Mena, E., Bertrán de Lis, S., Adibekyan, V. Z., et al. 2015, A&A, 576, A69
Delgado Mena, E., Israelian, G., González Hernández, J. I., et al. 2010, ApJ, 725, 2349
Delgado Mena, E., Israelian, G., González Hernández, J. I., et al. 2014, A&A, 562, A92
Ecuvillon, A., Israelian, G., Santos, N. C., et al. 2004, A&A, 426, 619
Figueira, P., Faria, J. P., Delgado-Mena, E., et al. 2014, A&A, 570, A21
Fischer, D. A., & Valenti, J. 2005, ApJ, 622, 1102
Gonzalez, G. 1997, MNRAS, 285, 403
Gonzalez, G. 1998, A&A, 334, 221
Gonzalez, G. 2014, MNRAS, 446, 1020
Gonzalez, G., Carlson, M. K., & Tobin, R. W. 2010, MNRAS, 407, 314
González Hernández, J. I., Delgado-Mena, E., Sousa, S. G., et al. 2013, A&A, 552, A6
González Hernández, J. I., Israelian, G., Santos, N. C., et al. 2010, ApJ, 720, 1592
Grevesse, N., Asplund, M., & Sauval, A. J. 2007, SSRv, 130, 105
Gustafsson, B., Karlsson, T., Olsson, E., Edvardsson, B., & Ryde, N. 1999, A&A, 342, 426
Hamer, J. H., & Schlaufman, K. C. 2019, AJ, 158, 190
Hawkins, K., Masseron, T., Jofré, P., et al. 2016, A&A, 594, A43
Howard, A. W., Marcy, G. W., Bryson, S. T., et al. 2012, ApJS, 201, 15
Israelian, G., Mena, E. D., Santos, N. C., et al. 2009, Natur, 462, 189
Johnson, D. R. H., & Soderblom, D. R. 1987, AJ, 93, 864
Johnson, J. A., Aller, K. M., Howard, A. W., & Crepp, J. R. 2010, PASP, 122, 905
Kobayashi, C., Karakas, A. I., & Lugaro, M. 2020, ApJ, 900, 179
Lee, Y. S., Beers, T. C., Sivarani, T., et al. 2008, AJ, 136, 2022
Luo, A., Zhang, J., Chen, J., et al. 2014, in IAU Symp. 298, Setting the Scene for Gaia and LAMOST, ed. S. Feltzing et al. (Cambridge: Cambridge Univ. Press), 428
Madhusudhan, N. 2012, ApJ, 758, 36
Manoj, P., & Bhatt, H. C. 2005, A&A, 429, 525
Mathur, S., Huber, D., Batalha, N. M., et al. 2017, ApJS, 229, 30
Mathur, S., Huber, D., Batalha, N. M., et al. 2018, ApJS, 234, 43
Meléndez, J., Asplund, M., Gustafsson, B., & Yong, D. 2009, ApJL, 704, L66
Meléndez, J., Bergemann, M., Cohen, J. G., et al. 2012, A&A, 543, A29
Mishenina, T., Kovtyukh, V., Soubiran, C., & Adibekyan, V. Z. 2016, MNRAS, 462, 1563
Mulders, G. D. 2018, in Planet Populations as a Function of Stellar, ed. H. J. Deeg & J. A. Belmonte (Berlin: Springer), 153
Mulders, G. D., Pascucci, I., Apai, D., Frasca, A., & Molenda-Żakowicz, J. 2016, AJ, 152, 187
Narang, M., Manoj, P., Furlan, E., et al. 2018, AJ, 156, 221
Neves, V., Santos, N. C., Sousa, S. G., Correia, A. C. M., & Israelian, G. 2009, A&A, 497, 563
Petigura, E. A., Marcy, G. W., Winn, J. N., et al. 2018, AJ, 155, 89
Plez, B. 2012, Turbospectrum: Code for spectral synthesis, Astrophysics Source Code Library, record ascl:1205.004
Pollack, J. B., Hubickyj, O., Bodenheimer, P., et al. 1996, Icar, 124, 62
Ramírez, I., Meléndez, J., & Asplund, M. 2009, A&A, 508, L17
Santos, N. C., Israelian, G., & Mayor, M. 2001, A&A, 373, 1019
Santos, N. C., Israelian, G., & Mayor, M. 2004, A&A, 415, 1153
Schlaufman, K. C., & Laughlin, G. 2011, ApJ, 738, 177
Sousa, S. G., Santos, N. C., Mayor, M., et al. 2008, A&A, 487, 373
Suárez-Andrés, L., Israelian, G., González Hernández, J. I., et al. 2017, A&A, 599, A96
Swastik, C., Banyal, R. K., Narang, M., et al. 2021, AJ, 161, 114
Swastik, C., Banyal, R. K., Narang, M., et al. 2022, AJ, 164, 60
Ujjwal, K., Kartha, S. S., Mathew, B., Manoj, P., & Narang, M. 2020, AJ, 159, 166
Youdin, A. N. 2011, ApJ, 742, 38
Zhao, G., Zhao, Y.-H., Chu, Y.-Q., Jing, Y.-P., & Deng, L.-C. 2012, RAA, 12, 723
Zong, W., Fu, J.-N., Cat, P. D., et al. 2018, ApJS, 238, 30